13. Schmidt-Kaler, F. *et al.* Realization of the Cirac-Zoller controlled-NOT quantum gate. *Nature* **422**, 408–411 (2003).
14. Leibfried, D. *et al.* Experimental demonstration of a robust, high-fidelity geometric two ion-qubit phase gate. *Nature* **422**, 412–415 (2003).
15. Mandel, O. *et al.* Controlled collisions for multi-particle entanglement of optically trapped atoms. *Nature* **425**, 937–940 (2003).
16. Julsgaard, B., Kozhekin, A. & Polzik, E. S. Experimental long-lived entanglement of two macroscopic objects. *Nature* **413**, 400–403 (2001).
17. Julsgaard, B., Sherson, J., Cirac, J. I., Fiurášek, J. & Polzik, E. S. Experimental demonstration of quantum memory for light. *Nature* **432**, 482–486 (2004).
18. Aspect, A., Grangier, P. & Roger, G. Experimental realization of Einstein-Podolski-Rosen-Bohm Gedankenexperiment: a new violation of Bell's inequalities. *Phys. Rev. Lett.* **49**, 91–94 (1982).
19. Kwiat, P. G., Waks, E., White, A. G., Appelbaum, I. & Eberhard, P. H. Ultrabright source of polarization-entangled photons. *Phys. Rev. A* **60**, R773–R776 (1999).
20. Kuklewicz, C. E., Fiorentino, M., Messin, G., Wong, F. N. C. & Shapiro, J. H. High-flux source of polarization-entangled photons from a periodically poled $KTiOPO_4$ parametric down-converter. *Phys. Rev. A* **69**, 013807 (2004).
21. Wootters, W. K. & Zurek, W. H. A single quantum cannot be cloned. *Nature* **299**, 802–803 (1982).
22. Tanzilli, S. *et al.* PPLN waveguide for quantum communication. *Eur. Phys. J. D* **18**, 155–160 (2002).
23. Banaszek, K., U'Ren, A. B. & Walmsley, I. A. Generation of correlated photons in controlled spatial modes by downconversion in nonlinear waveguides. *Opt. Lett.* **26**, 1367–1369 (2001).
24. Aspect, A. Bell's inequality test: more ideal than ever. *Nature* **398**, 189–190 (1999).
25. Franson, J. D. Bell inequality for position and time. *Phys. Rev. Lett.* **62**, 2205–2208 (1989).
26. Roussev, R. V., Langrock, C., Kurz, J. R. & Fejer, M. M. Periodically poled lithium niobate waveguide sum-frequency generator for efficient single-photon detection at communication wavelengths. *Opt. Lett.* **29**, 1518–1520 (2004).
27. Albota, M. A. & Wong, F. N. C. Efficient single-photon counting at 1.55 μm by means of frequency upconversion. *Opt. Lett.* **29**, 1449–1451 (2004).
28. Vandevender, A. P. & Kwiat, P. J. High efficiency single photon detection via frequency up-conversion. *J. Mod. Opt.* **51**, 1433–1445 (2004).
29. Marcikic, I., De Riedmatten, H., Tittel, W., Zbinden, H. & Gisin, N. Long-distance teleportation of qubits at telecommunication wavelengths. *Nature* **421**, 509–513 (2003).

Acknowledgements We thank D.B. Ostrowsky for discussions. Financial support by the Swiss Nation Center for Quantum Photonics and the European IST project RamboQ is acknowledged. S.T. acknowledges financial support from the European Science Foundation programme 'Quantum Information Theory and Quantum Computation'.

Author Information Reprints and permissions information is available at npg.nature.com/reprintsandpermissions. The authors declare no competing financial interests. Correspondence and requests for material should be addressed to S.T. (sebastien.tanzilli@physics.unige.ch).

Vol 437|1 September 2005|doi:10.1038/nature03968 nature

A general strategy for nanocrystal synthesis

Xun Wang[1,2], Jing Zhuang[1,2], Qing Peng[1,2] & Yadong Li[1,2]

New strategies for materials fabrication are of fundamental importance in the advancement of science and technology[1–12]. Organometallic[13,14] and other organic solution phase[15–17] synthetic routes have enabled the synthesis of functional inorganic quantum dots or nanocrystals. These nanomaterials form the building blocks for new bottom-up approaches to materials assembly for a range of uses; such materials also receive attention because of their intrinsic size-dependent properties and resulting applications[18–31]. Here we report a unified approach to the synthesis of a large variety of nanocrystals with different chemistries and properties and with low dispersity; these include noble metal, magnetic/dielectric, semiconducting, rare-earth fluorescent, biomedical, organic optoelectronic semiconducting and conducting polymer nanoparticles. This strategy is based on a general phase transfer and separation mechanism occurring at the interfaces of the liquid, solid and solution phases present during the synthesis. We believe our methodology provides a simple and convenient route to a variety of building blocks for assembling materials with novel structure and function in nanotechnology[1,2,29].

We chose noble metals as an example to demonstrate the effectiveness of this method in yielding high quality nanocrystals. Uniform noble metal quantum dots, or nanocrystals, can be obtained through the reduction of noble metal ions by ethanol at a temperature of 20 to 200 °C under hydrothermal or atmospheric conditions. In a typical synthesis, 20 ml of aqueous solution containing noble metal salts (for example, 0.5 g of $AgNO_3$, $HAuCl_4$ or other soluble chlorides), 1.6 g sodium linoleate, 10 ml ethanol and 2 ml linoleic acid were added to a 40 ml autoclave tube under agitation. The reactions were controlled at different temperatures for specific metals, for example, 80 to 200 °C for Ag, 20 to 200 °C for Ru, Rh and Ir, 20 to 100 °C for Au, Pd and Pt. The system was sealed and treated at the designated temperature for 10 hours. After the reaction was cooled to room temperature, the products were collected at the bottom of the vessel. Based on the same synthetic process, other fatty acid and corresponding salt systems can play the same roles as the linoleic acid system.

Figure 1a shows transmission electron microscope (TEM) images of typical samples of Ag, Au, Rh and Ir nanocrystals and indicates the large quantity and good uniformity (see Supplementary Information Part I and II) that were achieved using this approach. The Ag and Au nanocrystals are usually in round shapes with smooth surfaces, and self-assemble into ordered two-dimensional (2D) arrays on the surface of the TEM grid (Fig. 1a). The diameters of the nanocrystals can be reasonably tuned from about 4 to 15 nm by altering temperature, the mole ratio of the protecting reagents to noble metal ions or the chain length of the fatty acid (see Supplementary Information Part III). This approach has also been shown to yield the nearly monodisperse ultrafine metal nanocrystals of Ru, Rh, Ir, Pd and Pt with diameters of approximately 3 nm or less. Thorough high resolution (HR) TEM characterizations revealed the highly crystalline nature of these nanocrystals. Typical HRTEM images of Ir nanocrystals with diameters ~1.7 nm show an interplanar spacing of ~0.22 nm, which corresponds to the (111) planes of face-centred cubic Ir. EDS (energy dispersive spectroscopy) microanalysis and powder XRD (X-ray diffraction) (Fig. 2a) measurement have proven the successful synthesis of face-centred cubic structured Ag (JCPDS 4-783), Au (JCPDS 4-784), Pd (JCPDS 46-1043), Pt (JCPDS 4-802), Rh (JCPDS 5-685), Ir (JCPDS 46-1044) and hexagonal Ru (JCPDS 6-663).

The primary reaction in the preparation of noble metal nanocrystals through this liquid–solid–solution (LSS) process involved the reduction of noble metal ions by ethanol at the interfaces of metal linoleate (solid), ethanol–linoleic acid liquid phase (liquid) and water–ethanol solutions (solution) at different designated temperatures (Fig. 3). After the aqueous solution of noble metal ions, sodium linoleate (or another sodium stearate) and the mixture of linoleic acid (or another fatty acid) and ethanol were added into the vessel in order. Three phases formed in this system: sodium linoleate (solid), the liquid phase of ethanol and linoleic acid (liquid), and the water–ethanol solution containing noble metal ions (solution). A phase transfer process of the noble metal ions occurred spontaneously across the interface of sodium linoleate (solid) and the water–ethanol solution (solution) based on ion exchange, which led to the formation of noble metal linoleate and the entering of the sodium ions into the aqueous phases. Then at a designated temperature, the ethanol in the liquid and solution phases reduced the noble metal ions at the liquid–solid or solution–solid interfaces. Along with the reduction process, the *in-situ* generated linoleic acid absorbed on the surface of the noble metal nanocrystals with the alkyl chains on the outside, through which the produced metal nanocrystals will gain hydrophobic surfaces. A spontaneous phase-separation process then occurred because of the weight of the metal nanocrystals and the incompatibility between the hydrophobic surfaces and their hydrophilic surroundings, and the noble metal nanocrystals can be easily collected at the bottom of the container.

This LSS phase transfer and separation process can generate nanocrystals with a variety of properties such as, semiconducting, fluorescent, magnetic and dielectric. The phase transfer process can occur for nearly all the transitional or main group metal ions, which gives flexibility to the reactions at the interfaces (see Supplementary Information Part IV). After the phase transfer process of the metal ions from aqueous solution to the solid phase of $(RCOO)_nM$, under designated reaction conditions, the M^{n+} dehydrates into oxides (to yield for example, TiO_2, CuO, ZrO_2, SnO_2 or ZnO) and/or composite oxides (to yield for example, MFe_2O_4 (M represents Fe, Co, Mg, Zn or Mn) and $MTiO_3$ (M represents Ba or Sr) through co-precipitation). Alternatively, M^{n+} might react with other anion species such as S^{2-} (S^{2-} was supplied by Na_2S or $(NH_4)_2S$, to yield for example CdS, MnS, PbS, Ag_2S, CuS or ZnS), Se^{2-} (Se^{2-} was generated by the reduction of SeO_3^{2-} by N_2H_4, to yield for example CdSe or ZnSe) or F^- (F^- was provided from NaF or NH_4F, to yield for example YF_3, LaF_3 or $NaYF_4$) to yield various functional nanocrystals.

Nearly all the bandgap semiconductors can be effectively prepared through this simple LSS phase transfer and separation method, such

[1]Department of Chemistry, Tsinghua University, [2]National Center for Nanoscience and Nanotechnology, Beijing, 100084 China

as TiO_2, CuO, ZrO_2, SnO_2, CdS, Ag_2S, ZnS, PbS, MnS, ZnSe and CdSe. Representative TEM images of typical semiconductors of Ag_2S, PbS, ZnSe, CdSe and TiO_2 show the successful synthesis of various uniform semiconductor nanocrystals through this LSS approach (Fig. 1b, c). Two-dimensional assembly of PbS, Ag_2S, CuO, ZnSe and CdSe nanocrystals occurred spontaneously on the copper TEM grids after the evaporation of the solvents, indicating the regular shapes and narrow size distributions of these nanocrystals. Similar to the synthesis of noble metal nanocrystals, the size of the semiconductor nanocrystals can be tuned through several factors including temperature, mole ratio and the length of alkyl chains (see Supplementary Information Part III), however, for the synthesis of selenides, the temperature was controlled above 120 °C to ensure the complete reduction of SeO_3^{2-} by N_2H_4 (Fig. 2b). As mentioned above, the phase transfer process and control of the reactions at the different interfaces enabled the monodispersity and variability of the semiconductor nanocrystals obtained.

By adopting bi-metal precursors in a certain mole ratio, composite oxide nanocrystals such as magnetic MFe_2O_4 (M represents Fe, Co, Mg, Zn or Mn) and dielectric $MTiO_3$ (M represents Ba or Sr) can be effectively prepared through co-precipitation reactions following this LSS phase transfer and separation method. Uniform nanocrystals of magnetic spinel MFe_2O_4 could be prepared through the coprecipitation of Fe^{2+} ions and Fe^{3+}, Co^{2+}, Mg^{2+}, Mn^{2+} and Zn^{2+} ions. As shown in Fig. 1c, magnetic nanocrystals of Fe_3O_4 and $CoFe_2O_4$ with diameters ~10 nm formed 2D patterns on the TEM grids and showed good uniformity, which will be useful in biological labelling fields. In a similar way, the reaction between Ti^{4+} and Ba^{2+} and/or Sr^{2+} under strong alkali conditions can be used to prepare uniform nanocrystals of $BaTiO_3$ and $SrTiO_3$. Typical TEM and XRD analyses are shown in Fig. 1c and Fig. 2c, respectively, and show the formation of uniform nanocrystals of tetragonal $BaTiO_3$ (JCPDS 74-1960) with diameters ~17 nm.

Our LSS phase transfer and separation approach can also be used in generating nearly monodisperse rare earth fluorescent nanocrystals with up-conversion or down-conversion emission properties. These nanocrystals can also be prepared by tuning the reaction at the interfaces of the different phases. For example, after the phase transfer process of the rare earth ions, the reaction between NaF and the $(RCOO)_nLn$ generates LnF_3 ($NaYF_4$ in the case of Y; the reaction between NH_4F and Y^{3+} yields YF_3), whereas the reaction between OH^- and $(RCOO)_nLn$ generates $Ln(OH)_3$ nanocrystals (Fig. 2d).

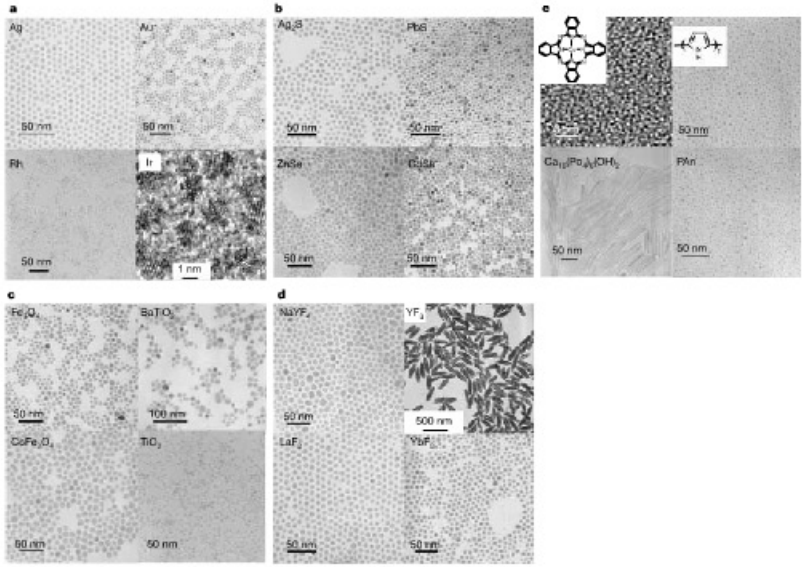

Figure 1 | TEM images of nanocrystals. **a**, Noble metal nanocrystals: Ag (6.1 ± 0.3 nm; 90 °C), Au (7.1 ± 0.5 nm; 50 °C), Rh (2.2 ± 0.1 nm; 120 °C) and Ir (1.7 ± 0.09 nm; 120 °C). **b**, Semiconductor nanocrystals: Ag_2S (7.3 ± 0.4 nm; 120 °C; Ag^+:S^{2-}, 2:1), PbS (5.7 ± 0.2 nm; Pb^{2+}:S^{2-}, 1:1), ZnSe (8.2 ± 0.9 nm; Zn^{2+}:SeO_3^{2-}, 1:1; 180 °C) and CdSe (7.1 ± 0.8 nm; Cd^{2+}:SeO_3^{2-}, 1:1; 180 °C). **c**, Magnetic and dielectric nanocrystals: Fe_3O_4 (9.1 ± 0.8 nm; Fe^{2+}:Fe^{3+}, 1:2; 160 °C), $CoFe_2O_4$ (11.5 ± 0.6 nm; Co^{2+}:Fe^{3+}, 1:2; 180 °C), $BaTiO_3$ (16.8 ± 1.7 nm; 7 g NaOH for 0.5 g $Ba(NO_3)_2$ and equal amount of $TiCl_3$ (in mole ratio); 180 °C; Ti^{3+} have been adopted as Ti sources because of the relative stability of Ti^{3+} to Ti^{4+} under aqueous conditions, which will be oxidized into Ti^{4+} under hydrothermal conditions) and TiO_2 (4.3 ± 0.2 nm; 1 ml 30% $TiCl_3$ solution for 40 ml vessel; 180 °C). **d**, Rare earth fluorescence nanocrystals: $NaYF_4$ (10.5 ± 0.7 nm; NaF:Y^{3+}, 4:1, 180 °C), YF_3 (NH_4F:Y^{3+}, 3:1, 180 °C), LaF_3 (8.0 ± 0.3 nm; F^-:La^{3+}, 3:1, 180 °C), YbF_3 (9.5 ± 0.6 nm; F^-:Yb^{3+}, 3:1, 180 °C). **e**, TEM images of $Ca_{10}(PO_4)_6(OH)_2$, Ppy (4.2 ± 0.5 nm), PAn (3.3 ± 0.5 nm) and copper phthalocyanine (0.8 ± 0.1 nm) nanocrystals.

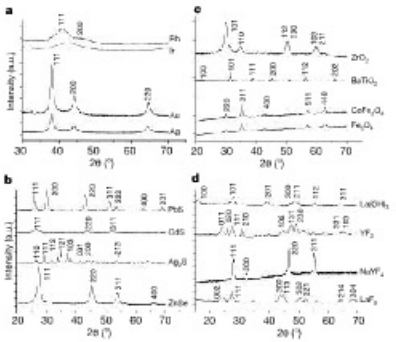

Figure 2 | XRD patterns of nanocrystals. **a**, Noble metal nanocrystals: Au, Ag, Rh and Ir. **b**, Semiconductor nanocrystals: monoclinic Ag_2S (JCPDS 14-0072), face-centred cubic PbS (JCPDS 5-592), ZnSe (JCPDS 80-21) and face-centred cubic CdS (JCPDS 75-0581). **c**, Magnetic and dielectric nanocrystals: Fe_3O_4 (JCPDS 76-1849), $CoFe_2O_4$ (JCPDS 79-1744), tetragonal $BaTiO_3$ (JCPDS 74-1960) and ZrO_2. **d**, Rare earth fluorescence nanocrystals: $NaYF_4$ (JCPDS 77-2042), YF_3 (JCPDS 74-911), LaF_3 (JCPDS 72-1435) and $La(OH)_3$ (JCPDS 36-1481).

Figure 1d shows the TEM figures of $NaYF_4$, YF_3, LaF_3 and YbF_3 nanocrystals. $NaYF_4$, YbF_3 and LaF_3 are approximately round, with a diameter in the range of 4–12 nm (that varies with temperature), whereas YF_3 is characterized as having a rice-like shape with a diameter ~100 nm and length ~500 nm (composed of uniform nanocrystals with a diameter ~5 nm). $Ln(OH)_3$ products are usually composed of uniform nanorods with a diameter 3–15 nm (that varies with temperature). By doping different rare earth ions such as Eu^{3+}, Tb^{3+} or Yb/Er these nanocrystals were functional as fluorescence nanocrystals (see Supplementary Information part V).

Along with the series of functional nanocrystals mentioned above, this LSS strategy also shows great potential in the synthesis of a broad range of new-type nanocrystals and/or nanoparticles (see Supplementary Information part VI). This will provide new materials for wide research areas including biocompatible materials, organic optoelectronic semiconductors, nanomedicine as well as conducting polymers. For example, the monodisperse biocompatible hydroxyapatite ($Ca_{10}(PO_4)_6(OH)_2$) nanorods (Fig. 1e, bottom left), which as a raw material may find an application in the preparation of artificial bone grafts because of its uniformity and nanometre size. Also, the typical conducting polymer nanocrystals of PPy and PAn (Fig. 1e, right), may provide an ideal model for the investigation of nano-size effects in the conducting polymer field. Finally, metal (copper in this case) phthalocyanine nanocrystals (Fig. 1e, top left) obtained following this LSS procedure, can be further investigated as an optoelectronic nanomaterial. Therefore, by properly tuning the chemical reactions at the interfaces, we believe that more interesting and important new-type nanocrystals can be obtained.

All the nanocrystals (such as noble metal, magnetic, dielectric, semiconducting and rare earth fluorescence), and other new type (such as, monodisperse biomedical, organic optoelectronic semiconductors and conducting polymers) nanoparticles, can be easily dispersed in nonpolar solvents (such as, cyclohexane or chloroform) to form homogenous colloidal solutions (Fig. 4), which are usually stable for months. By dropping the solution on the surface of a

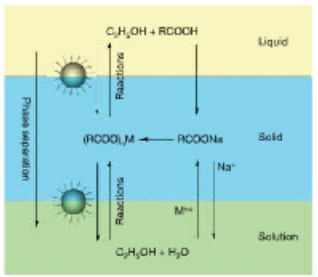

Figure 3 | Scheme of liquid–solid–solution (LSS) phase transfer synthetic strategy.

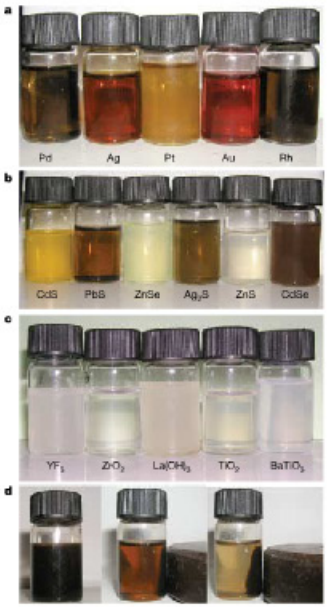

Figure 4 | Cyclohexane solutions of nanoparticles with a typical concentration of 2%. **a**–**d**, Cyclohexane solutions of noble metal (**a**), semiconductors (**b**), rare earth fluorescence (**c**) and magnetic nanocrystals (**d**). **d**, The separation of $CoFe_2O_4$ nanocrystals from the bulky solution by magnetic force.

Vol 437|1 September 2005|doi:10.1038/nature03975 nature

substrate or through a dip-coating technique, monolayer films of functional nanocrystals could be easily obtained, which will greatly increase their application in nanoscience and technology. These nanocrystals could also be re-precipitated and separated by adding an appropriate amount of ethanol to the bulky nanocrystals solutions or by force due to an external field and show advantages in processing. All these disperse/separation characteristics of the functional nanocrystals obtained through this LSS approach will provide the building blocks for the bottom-up approach to nanoscale fabrication in nanosciences and nanotechnologies.

Received 18 May; accepted 23 June 2005.

1. Kroto, H. W., Heath, J. R., O'Brien, S. C., Curl, R. F. & Smalley, R. E. C60: Buckminsterfullerene. *Nature* **318,** 162–163 (1985).
2. Iijima, S. Helical microtubules of graphitic carbon. *Nature* **354,** 56–58 (1991).
3. Morales, A. M. & Lieber, C. M. A laser ablation method for the synthesis of crystalline semiconductor nanowires. *Science* **279,** 208–211 (1998).
4. Huang, M. H. *et al.* Room-temperature ultraviolet nanowire nanolasers. *Science* **292,** 1897–1899 (2001).
5. Tenne, R., Margulis, L., Genut, M. & Hodes, G. Polyhedral and cylindrical structures of Tungsten disulfide. *Nature* **360,** 444–446 (1992).
6. Pan, Z. W., Dai, Z. R. & Wang, Z. L. Nanobelts of semiconducting oxides. *Science* **291,** 1947–1949 (2001).
7. Duan, X. F., Huang, Y., Cui, Y., Wang, J. F. & Lieber, C. M. Indium phosphide nanowire as building blocks for nanoscale electronic and optoelectronic devices. *Nature* **409,** 66–69 (2001).
8. Huang, Y., Duan, X. F., Wei, Q. Q. & Lieber, C. M. Directed assembly of one-dimensional nanostructures into functional networks. *Science* **291,** 630–633 (2001).
9. Law, M. *et al.* Nanoribbon waveguides for subwavelength photonics integration. *Science* **305,** 1269–1273 (2004).
10. Beck, J. S. *et al.* A new family of mesoporous molecular sieves prepared with liquid crystal templates. *J. Am. Chem. Soc.* **114,** 10834–10843 (1992).
11. Huo, Q. S. *et al.* Generalized syntheses of periodic surfactant inorganic composite-materials. *Nature* **368,** 317–321 (1994).
12. Yang, P. D., Zhao, D. Y., Margolese, D. I., Chmelka, B. F. & Stucky, G. D. Generalized syntheses of large-pore mesoporous metal oxides with semicrystalline frameworks. *Nature* **396,** 152–155 (1998).
13. Murray, C. B., Norris, D. J. & Bawendi, M. G. Synthesis and characterization of nearly monodisperse CdE (E = sulfur, selenium, tellurium) semiconductor nanocrystallites. *J. Am. Chem. Soc.* **115,** 8706–8715 (1993).
14. Peng, X. G. *et al.* Shape control of CdSe nanocrystals. *Nature* **404,** 59–61 (2000).
15. Sun, S. H., Murray, C. B., Weller, D., Folks, L. & Moser, A. Monodisperse FePt nanoparticles and ferromagnetic FePt nanocrystal superlattices. *Science* **287,** 1989–1992 (2000).
16. Murray, C. B., Kagan, C. R. & Bawendi, M. G. Self organization of CdSe nanocrystallites into 3-dimentional quantum-dot superlattices. *Science* **270,** 1335–1338 (1995).
17. Sun, Y. G. & Xia, Y. N. Shape-controlled synthesis of gold and silver nanoparticles. *Science* **298,** 2176–2179 (2002).
18. Jovin, T. M. Quantum dots finally come of age. *Nature Biotechnol.* **21,** 32–33 (2003).
19. Huynh, W. U., Dittmer, J. J. & Alivisatos, A. P. Hybrid nanorod-polymer solar cells. *Science* **295,** 2425–2427 (2002).
20. Tessler, N., Medvedev, V., Kazes, M., Kan, S. H. & Banin, U. Efficient near-infrared polymer nanocrystal light-emitting diodes. *Science* **295,** 1506–1508 (2002).
21. Klimov, V. I. *et al.* Optical gain and stimulated emission in nanocrystal quantum dots. *Science* **290,** 314–317 (2000).
22. Li, Y. D. *et al.* Bismuth nanotubes: A rational low-temperature synthetic route. *J. Am. Chem. Soc.* **123,** 9904–9905 (2001).
23. Li, Y. D., Li, X. L., He, R. R., Zhu, J. & Deng, Z. X. Artificial lamellar mesostructures to WS2 nanotubes. *J. Am. Chem. Soc.* **124,** 1411–1416 (2002).
24. Wang, X. & Li, Y. D. Selected-control hydrothermal synthesis of alpha- and beta-MnO2 single crystal nanowires. *J. Am. Chem. Soc.* **124,** 2880–2881 (2002).
25. Wang, X. & Li, Y. D. Synthesis and characterization of lanthanide hydroxide single-crystal nanowires. *Angew. Chem. Int. Edn Engl.* **41,** 4790–4793 (2002).
26. Peng, Q., Dong, Y. J. & Li, Y. D. ZnSe semiconductor hollow microspheres. *Angew. Chem. Int. Edn Engl.* **42,** 3027–3030 (2003).
27. Wang, X. & Li, Y. D. Fullerene-like rare-earth nanoparticles. *Angew. Chem. Int. Edn Engl.* **42,** 3497–3500 (2003).
28. Wang, X., Zhuang, J., Chen, J., Zhou, K. B. & Li, Y. D. Thermally stable silicate nanotubes. *Angew. Chem. Int. Edn Engl.* **43,** 2017–2020 (2004).
29. Sun, X. M. & Li, Y. D. Ga2O3 and GaN semiconductor hollow spheres. *Angew. Chem. Int. Edn Engl.* **43,** 3827–3831 (2004).

Supplementary Information is linked to the online version of the paper at www.nature.com/nature.

Acknowledgements This work was supported by NSFC, the Foundation for the Author of National Excellent Doctoral Dissertation of China and the State Key Project of Fundamental Research for Nanomaterials and Nanostructures.

Author Information Reprints and permissions information is available at npg.nature.com/reprintsandpermissions. The authors declare no competing financial interests. Correspondence and requests for materials should be addressed to L.Y. (ydli@tsinghua.edu.cn).

Modelled atmospheric temperatures and global sea levels over the past million years

Richard Bintanja[1], Roderik S.W. van de Wal[1] & Johannes Oerlemans[1]

Marine records of sediment oxygen isotope compositions show that the Earth's climate has gone through a succession of glacial and interglacial periods during the past million years. But the interpretation of the oxygen isotope records is complicated because both isotope storage in ice sheets and deep-water temperature affect the recorded isotopic composition[1–3]. Separating these two effects would require long records of either sea level or deep-ocean temperature, which are currently not available. Here we use a coupled model of the Northern Hemisphere ice sheets[4] and ocean temperatures, forced to match an oxygen isotope record for the past million years compiled from 57 globally distributed sediment cores, to quantify both contributions simultaneously. We find that the ice-sheet contribution to the variability in oxygen isotope composition varied from ten per cent in the beginning of glacial periods to sixty per cent at glacial maxima, suggesting that strong ocean cooling preceded slow ice-sheet build-up. The model yields mutually consistent time series of continental mean surface temperatures between 40 and 80° N, ice volume and global sea level. We find that during extreme glacial stages, air temperatures were 17 ± 1.8 °C lower than present, with a 120 ± 10 m sea level equivalent of continental ice present.

Marine oxygen isotope records have provided detailed information about climatic variations over the past millions of years[5]. Interpreting the fluctuations in oxygen isotope ($\delta^{18}O$ ratio) is not straightforward, however, because the signal is affected mainly by two mechanisms (aside from local hydrographical influences). The first is preferential evaporation and subsequent incorporation of the lighter oxygen isotope in ice sheets during glacial conditions, which affects the ocean's $\delta^{18}O$ value (the 'ice-sheet part'). The second mechanism is mainly related to the uptake of $\delta^{18}O$ in calcite by benthic foraminifera, which depends on local deep-water temperature at the time of crystallization of their shells[6] (the 'deep-water part'). Previous attempts to separate these two effects involved the use of independent temperature and sea-level records to estimate either the ice-sheet part[7,8] or the deep-water part[3]. Albeit with considerable uncertainty, owing mainly to local water-mass variability, these studies have yielded long (several 100,000 yr, or 100 kyr) combined records of sea level and deep-sea temperature. These showed that the glacial deep ocean was 2–3 °C colder than today, which agrees with temperatures inferred from the Mg/Ca ratio in fossil ostracodes[10].

We have tried a different approach, one that takes advantage of the fact that on glacial–interglacial timescales, the main contributors to the mean benthic oxygen isotope record—the Northern Hemisphere ice-sheet isotope content and the local deep-sea temperature—are both strongly related to Northern Hemisphere midlatitude to subpolar surface air temperature. This puts constraints on the surface air temperature, which enabled us to separate the ice-sheet and deep-water parts simultaneously and consistently, without the need to know either in advance. Based only on $\delta^{18}O$ data, our method additionally provides reconstructions of actual climate variables such as surface air temperature, global sea level and ice volume and ice isotope content.

Ideally, the reconstructions should be as generally representative as possible, which can be achieved by an appropriate choice of input $\delta^{18}O$ record. Many long records of benthic $\delta^{18}O$ exist today, all carrying global information, but superimposed on their global signal is the unknown effect of local hydrographical effects[3]. This variability would introduce unfavourable uncertainty in the reconstructions. For this reason, we selected a recently developed benthic $\delta^{18}O$ stack based on 57 globally distributed records[11], to drive our ice-sheet–ocean-temperature model (results for two individual records are shown in the Supplementary Information). In this stack, we assume

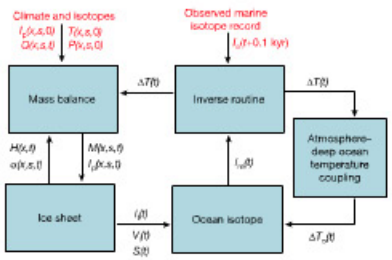

Figure 1 | Schematic outline of the inverse procedure. The routine calculates a mean surface air temperature anomaly (ΔT) based on the difference between the modelled marine isotope value ($I_m(t)$) and the observed value 0.1 kyr later ($I_o(t + 0.1\ \mathrm{kyr})$). The value of ΔT feeds into two physical systems: (1) the ice-sheet and mass-balance module to the left and (2) the atmosphere–deep ocean temperature coupling module to the right. The mass-balance module calculates spatially (x), seasonally (s) and temporally (t) varying fields of surface mass balance (M) and isotope content of precipitation (I_p) using initial, present-day (0) fields of I_p, surface air temperature (T) and precipitation (P) and temporally varying orbitally induced insolation (Q). M and I_p are used by the ice-sheet module to calculate new distributions of ice-sheet surface height (H) and surface albedo (α), which feed back into the mass balance routine. The ice-sheet routine determines the mean ice-sheet isotope content (I_i), the ice-sheet volume (V_i) and global sea level (S). These values, together with the deep-ocean temperature (ΔT_o), are used by the ocean routine to evaluate the marine isotope value (I_m) that feeds into the inverse routine. This procedure yields mutually consistent time series of ΔT, ΔT_o, V_i, S, and I_i. Observed (input) variables are in red, modelled ones in black.

[1]Institute for Marine and Atmospheric Research Utrecht, Utrecht University, Princetonplein 5, 3584 CC Utrecht, The Netherlands.